



Chinese Society of Aeronautics and Astronautics  
& Beihang University

Chinese Journal of Aeronautics

cja@buaa.edu.cn  
[www.sciencedirect.com](http://www.sciencedirect.com)



# Investigations on MBSE modelling and dynamic performance assessment of an electrical trimmable horizontal stabilizer actuator

Wensen ZHANG<sup>a</sup>, Jian FU<sup>a</sup>, Jean-Charles MARÉ<sup>b</sup>, Haolin MA<sup>a</sup>,  
Tianxiang XIA<sup>c</sup>, Yongling FU<sup>a</sup>, Jiangao ZHAO<sup>a,\*</sup>

<sup>a</sup> School of Mechanical Engineering and Automation, Beihang University, Beijing 100191, China

<sup>b</sup> INSA – Institut Clément Ader (CNRS UMR 5312), Toulouse 31400, France

<sup>c</sup> Nanjing Engineer Institute of Aircraft System Jincheng, AVIC, Nanjing 211100, China

Received 8 November 2022; revised 13 January 2023; accepted 21 February 2023

Available online 5 April 2023

## KEYWORDS

Electro-mechanical actuator;  
Flight control;  
Mechanical load path;  
Modelling;  
No-back mechanism

**Abstract** With the development of power-by-wire technology for more electric aircraft, the electro-mechanical actuator (EMA) has the advantages to replace the conventional hydraulic servo actuator in some aerospace flight controls. Conventional hydraulically powered trimmable horizontal stabilizer actuation (THSA) system is nowadays developed to be electrically supplied. Given their safety-criticality, no-back mechanism and redundant load paths are utilized to meet the flight control requirements. However, rare literatures have introduced these functions and addressed the virtual prototyping activities from system-level point of view. This paper proposed such a model of a THSA system with dual electric power sources and fault-tolerant mechanical load paths. The non-linear effects of components are considered with realism, and system-level simulation test is conducted to support the model-based system engineering (MBSE) approach. The models are developed with a power view instead of a pure signal view. Focusing on the friction effect and compliance effect with backlash or preload, some improved and novel approaches are adopted for these crucial components and validated via experimental results. Meanwhile, the implemented system-level model enables injection of crucial faults. Finally, the simulation of the proposed model shows

\* Corresponding author.

E-mail address: [jazhao@buaa.edu.cn](mailto:jazhao@buaa.edu.cn) (J. ZHAO).

Peer review under responsibility of Editorial Committee of CJA.



Production and hosting by Elsevier

## Nomenclature

Symbol	Item	
$b_{pb}$	Primary load path backlash, mm	$k_{p,1}$ Stiffness between lower no-back components ( $\text{N}\cdot\text{m}^{-1}$ )
$b_{rn}$	Secondary nut assembly backlash mm	$k_{p,u}$ Stiffness between upper no-back components ( $\text{N}\cdot\text{m}^{-1}$ )
$b_{tb}$	Tie bar assembly backlash mm	$k_{sn}$ Stiffness between screw-nut mechanism ( $\text{N}\cdot\text{m}^{-1}$ )
$d_g$	Gear contact damper rating $\text{N}\cdot\text{m}\cdot\text{rad}^{-1}\cdot\text{s}$	$k_t$ Motor torque constant ( $\text{N}\cdot\text{m}\cdot\text{A}^{-1}$ )
$d_p$	Contact damper rating between ratchet and pawl ( $\text{N}\cdot\text{m}\cdot\text{rad}^{-1}\cdot\text{s}$ )	$l_s$ Lead of screw (mm)
$d_{pb}$	Damper rating between no-back components ( $\text{N}\cdot\text{m}^{-1}\cdot\text{s}$ )	$L_s$ Stator inductance (mH)
$d_{sn}$	Damper rating between screw-nut mechanism ( $\text{N}\cdot\text{m}^{-1}\cdot\text{s}$ )	$m_b$ Mass of recirculating balls (kg)
$f_c$	Coulomb friction coefficient of screw-nut	$m_{hs}$ Equivalent mass of THS (reflected at nut)(kg)
$F_L$	Load force (N)	$m_{st}$ Equivalent mass of screw and tie bar (kg)
$F_n$	Axial output force on nut (N)	$m_{ug}$ Equivalent mass of upper gimbal components (kg)
$F_p$	Initial preload force (N)	$R_e$ Circle radius of the contact point (mm)
$F_{st}$	Axial force transmitted by screw shaft (N)	$R_s$ Stator resistance ( $\Omega$ )
$f_v$	Motor viscous friction coefficient ( $\text{N}\cdot\text{m}\cdot\text{rad}^{-1}\cdot\text{s}$ )	$T_n$ Rated motor torque ( $\text{N}\cdot\text{m}$ )
$i$	Total gear ratio	$T_{rw}$ Freewheeling friction torque ( $\text{N}\cdot\text{m}$ )
$I_{max}$	Maximum phase current (A)	$T_{POB}$ POB constant torque ( $\text{N}\cdot\text{m}$ )
$J_m$	Inertia of rotor ( $\text{kg}\cdot\text{m}^2$ )	$T_s$ Screw driving torque ( $\text{N}\cdot\text{m}$ )
$J_{rw}$	Ratchet wheel inertia ( $\text{kg}\cdot\text{m}^2$ )	$U_{dc}$ DC bus voltage (V)
$J_s$	Screw shaft inertia ( $\text{kg}\cdot\text{m}^2$ )	$x_{st}$ Additional displacement caused by load path compliance (mm)
$k_{ds}$	Stiffness of preload disk spring ( $\text{N}\cdot\text{m}^{-1}$ )	$\beta$ Contact angle of screw (deg)
$k_g$	Gear contact stiffness ( $\text{N}\cdot\text{m}\cdot\text{deg}^{-1}$ )	$\mu_c$ Coulomb friction coefficient (m)
$k_p$	Contact stiffness between ratchet and pawl ( $\text{N}\cdot\text{m}\cdot\text{deg}^{-1}$ )	$\mu_s$ No-back stick friction coefficient (m)
		$\omega_s$ Screw velocity (r/min)
		$\omega_{st}$ Stribeck velocity constant (r/min)

that it is an efficient resource to investigate the actuator's dynamic performance, to virtually prove that the actuator meets the fail-safe constraint, and to demonstrate the soundness of the fault monitoring functions.

© 2023 Production and hosting by Elsevier Ltd. on behalf of Chinese Society of Aeronautics and Astronautics. This is an open access article under the CC BY-NC-ND license (<http://creativecommons.org/licenses/by-nc-nd/4.0/>).

## 1. Introduction

With the development of more electric aircraft or all electric aircraft, the application of power-by-wire (PbW) actuators has become a major target.<sup>1,2</sup> The PbW technology removes the centralized hydraulic power generation and distribution, which is advantageous for power management, integration, and maintenance.<sup>3</sup> Two categories PbW actuators, which are respectively named as electro-hydrostatic actuator (EHA) and EMA are came already to service in commercial civil aircrafts. EHAs still use hydraulics locally,<sup>4,5</sup> whereas EMAs (Fig. 1) remove both central and local hydraulic circuits with resort to a pure mechanical power transmission between the motor and the driven load.<sup>6</sup> Thus, EMAs can achieve possibly higher power transmission efficiency and superior resistance to pollution than EHAs. However, without utilizing hydraulic oil as transmission medium, it requires more serious design considerations at thermal effect. In case of jamming fault, EMA is difficult to isolate this fault, whereas EHAs can easily overcome this problem by using a bypass valve. And that is why

only EHAs are in service for primary flight controls nowadays.<sup>3,7</sup>

Although EMAs are not yet mature enough for primary flight controls because of their risk of jamming, they can be successfully used for secondary flight controls, in particular for trimming the horizontal stabilizer, Fig. 1 (a),<sup>7</sup> for which the preferred response to fault is fail-frozen. At this situation, EMA seems to be a superior option than EHA. And Nowadays, EMA has been successfully utilized as trimmable horizontal stabilizer actuator in A350 and B787 for auxiliary pitch control.<sup>8</sup> Compared to conventional EMA architecture for flight control system in Fig. 1 (b), such actuators generally involve a torque limiter and no-back mechanism for overload protection and irreversibility, respectively.

However, the introduction of electrical actuation for trimmable horizontal stabilizer (THS) raises new challenges for virtual prototyping and testing, where power sizing, back-drivability, cushioning and damping, response to failures and heat rejections are major concerns.<sup>3,9</sup> In such a situation, the MBSE approach can provide engineers with efficient means

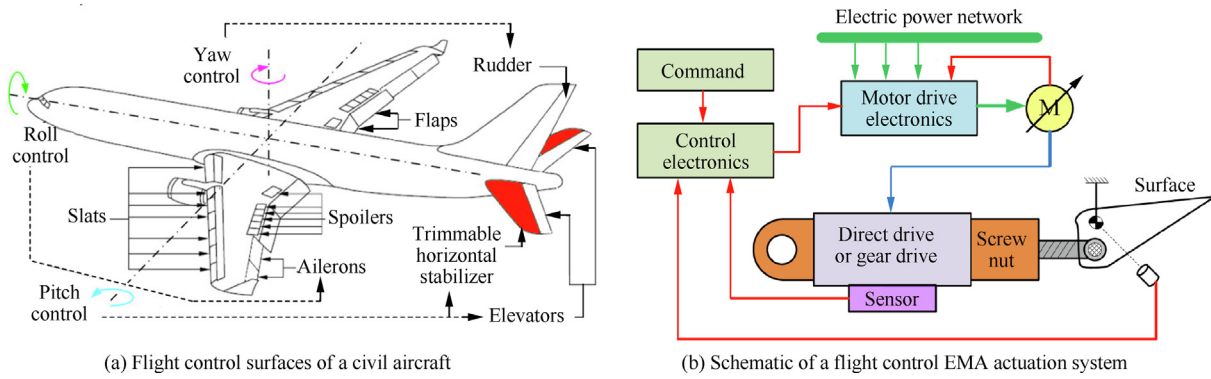


**Fig. 1** PbW technology for trimmable horizontal stabilizer actuation.

to address all these major considerations as a whole at reduced costs and risk.<sup>10</sup> By developing and validating realistic component models and running system-level virtual tests, engineers can benchmark the different architectural choice and run efficiently optimization and robustness studies. This undoubtfully supports and accelerates most of major engineering tasks, such as control design, component sizing, thermal management, and function pre-validation.<sup>11,12</sup>

Some relevant researches on EMA modelling have been conducted earlier. Fu et al. developed a system-level EMA model with considerations on multidisciplinary effects via Bond-Graph formalism.<sup>13</sup> Karam et al. provided an EMA model with special focus on the compliance effect and friction effect in mechanical transmission.<sup>14</sup> This reference proposes a representation model of friction, identified from real experiments, that accounts for friction dependence on load, velocity and operating quadrant inside the roller-screw mechanism. However, both these studies focused on a direct driven EMA without any electrical and mechanical load path redundancy, which does not meet the reliability targets of a THSA. Arriola et al. built an aileron actuation system model consisting of dual individual EMAs to verify a fault monitoring concept. The backlash of the mechanical transmission is focused whereas friction is simply modelled using efficiency parameter.<sup>15</sup> Giangrande et al. provided a redundant solution for secondary flight controls with an EMA driven by dual motors. However, the physical effects and fault-tolerant function of motor and electric drive elements are considered, rather than mechanical components.<sup>16</sup> Bertolino et al. proposed a realistic model with lumped parameters for ball-screw mechanism considering normal compliance effect and tangential slip friction.<sup>17</sup> The functions and operation principles of torque limiter and no-back mechanism have been already documented,<sup>18</sup> whereas their system-level modelling almost never addressed with a power view.

The successful application of the MBSE approach in the THSA development process relies on realistic component models and system-level simulation test, including virtual integration. This paper reports research on model implementation methodology and experimental validation, which contributes to this goal. Therefore, the virtual prototyping of some safety-critical designs, such as electrical and mechanical load path redundancy, screw-nut mechanism and no-back mechanism, is conducted. In addition, the established model considers the nonlinear effects, which may show significant impact on

system performance, and enables the fault monitoring and fault tolerance verification to be performed.

This paper is organized as follows. In section 2, the architecture of a fault-tolerant THSA is analyzed. Section 3, the components are modelled with the work principle analysis, paying particular attention to nonlinear effects, like friction, compliance with backlash or preload. Section 4 illustrates how the modelling proposals can be implemented in a commercial simulation environment. In Section 5, combining the simulation and experimental results, the modelling approach and the importance of considering the nonlinear effects is verified. Finally, the conclusion summarizes the main contributions.

## 2. System description

With respect to THSA for safety-critical embedded actuation applications, proposing an appropriate architecture is required to satisfy the flight control system requirements.<sup>6,19</sup> As shown schematically in Fig. 2, the adopted actuation architecture comprises the following components:

**Motor and brake assembly (MBA):** The THSA involves a primary MBA and a backup MBA, which are combined using the torque summing concept. Functionally speaking, the backup MBA, when operating in passive mode, offers no resistance to the primary MBA in active mode. Dual MBAs can be alternately utilized in variable flight missions. The power-off brake (POB) performs a secondary brake function, which enables to lock the THS in position. More importantly, both POBs engage simultaneously, if either is electrically energized.

**Motor control electronics (MCE):** MCE is in charge of supplying the electrical motor (EM) with adequate voltage magnitude, phase and frequency. It acts as a power transformer between the electric supply and the motor, which is modulated by the control signal.

**EMCU:** Based on the motor speed feedback and trim speed command from flight control computer (FCC), velocity loop regulation and current command generation for MCE are executed through the EMCU. The EMCU is also responsible for fault diagnosis with specific strategies. For this purpose, it uses the signals sampled from the various THSA sensors, such as linear variable displacement transducer (LVDT), rotary variable displacement transducer (RVDT), etc.<sup>20</sup> The diagnosis results are interacted with FCC to disengage the defective actuation channel.

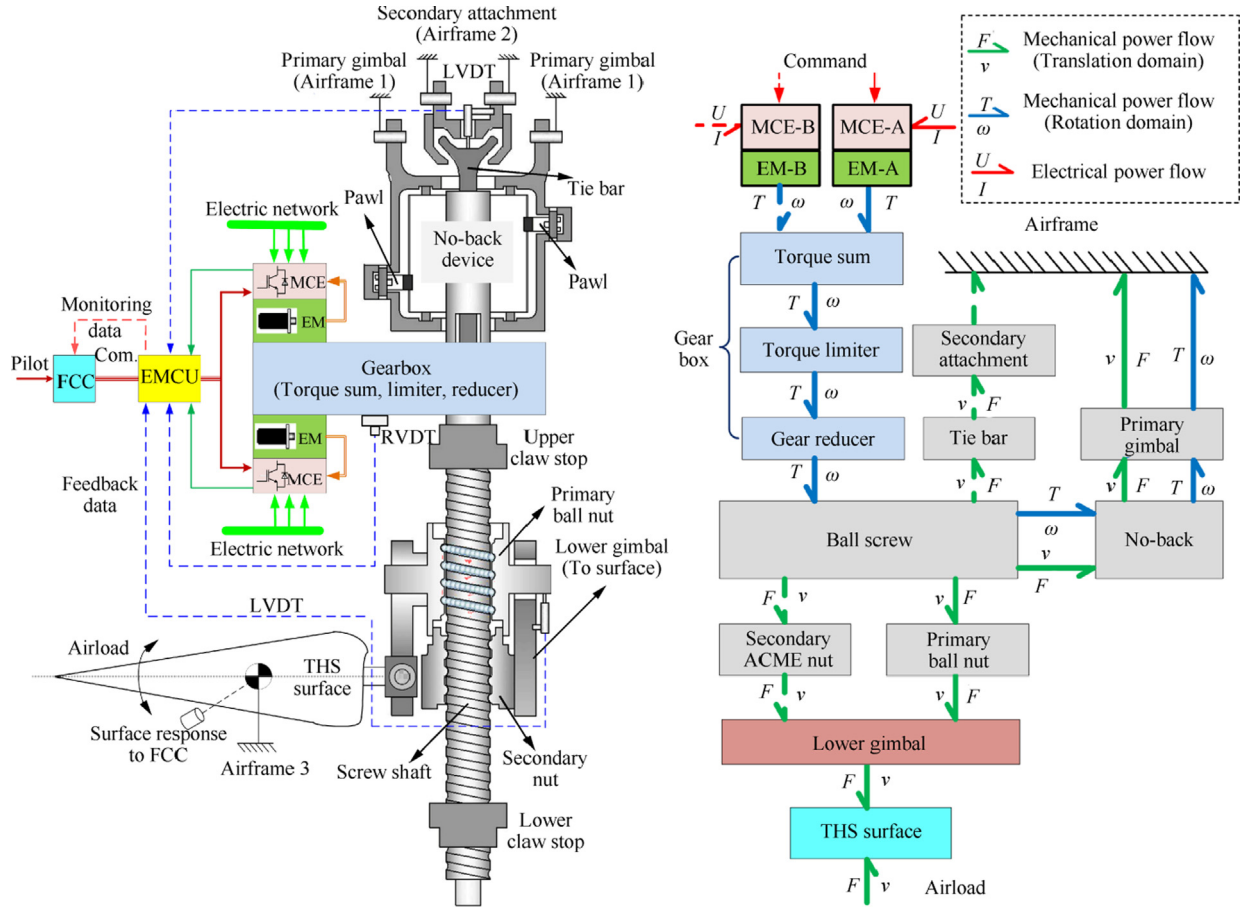


**Fig. 2** Architecture and power flow paths of THSA system.

**Gearbox:** In addition to the main velocity reduction function, the gearbox integrates internally a torque limiter, which is responsible for motor protection under overload situation. Dual RVDTs, installed on gearbox and backup each other, feedback the current THS position to the FCC through the EMCU for monitoring and fault processing purposes.

**Screw-nut mechanism:** The rotary motion of the screw (driven by the active motor) is transformed into linear motion of the nut (attached to the THS with a redundant gimbal). The active motion is finally converted into the THS rotation angle around pivot.

**Mechanical load path:** The mechanical load path enables the THS to transmit the axial force between the airframe and the THSA. It is made totally redundant (active/standby) thanks to the primary and secondary gimbals (anchorage of the THSA to the airframe), the screw and tie bar (transmission of axial loads internally to the THS), the redundant nut, and the lower gimbals (attached to the THS). The respective components are illustrated and distinguished with different colors in Fig. 2.

**No-back device:** the fundamental function of no-back mechanism is to make the THSA irreversible. When the THS operates in aiding load conditions, and in the absence of operation of the THSA, it brakes the screw shaft against the housing of the THSA.

Despite of the similar EMA architecture has been successfully utilized in present civil aircraft, there still exist some potential limitations. Firstly, to meet the reliability and fault-

tolerant requirements by a single EMA, the actuator architecture must utilize enough component redundancies and essential safety-critical devices, such as torque limiter, no-back mechanism. The complex redundancy configuration and mechanical construction lead to low power-to-weight ratio and bring more design risks. Secondly, the preferred response to mechanical fault for THSA is fail-frozen, which implies the loss of normal actuation function. Therefore, in this situation, the pitch control function will be influenced by only relying on the elevator flight control system.

As depicted in Fig. 2, the power flow paths between actuator components indicate the power categories and directions. The power flows of voltage and current for electrical domain are translated into mechanical domain via electrical motor. The mechanical power flow is further divided into translation and rotation domain, and the transform is completed by utilizing the gearbox and screw-nut mechanism. Meanwhile, the rotation and translation power flows provide an explicit representation of how motor torque and axial load force are transmitted among these components during operation.

### 3. System-level modelling of physical effects

To achieve system-level modelling, the subsequent work is to conduct the modelling principle analysis of each crucial component. It is important to note that the physical effects of THSA are involved in multiple complex nonlinear factors: saturation, friction, backlash and preload in compliance effect,

etc., and multiple domains: electrical, magnetic, mechanical and thermal. It is noted that it is not intended to build a 6DOF model with all inertia and joint compliance matrix. Only the physical effects showing influence on rotation freedom around screw axis and axial freedom will be considered. Any less important inertia and compliance effect will be neglected or merged to another component. The physical effect descriptions and modelling approaches of MCE and EM have been detailed addressed in previous research<sup>21</sup> and will not be repeated. The gearbox acts functionally as a mechanical power transformer. The torque limiter transmits torque through friction, and can saturate the transmitted torque to the torque amplitude produced from friction disks.

### 3.1. Screw-nut mechanism

The most common basic model of a screw-nut mechanism performs as a perfect rotary/linear power transformation element, where the friction loss is defined by a constant efficiency parameter. And early research has established a bond graph model,<sup>22</sup> which applied well to screw-nut where the tangent plane of contact is the thread. The power is functionally transmitted by forces acting perpendicularly to contact. The friction losses appear as tangential forces in the tangential path. In the present research, the modelling principle will be referred and modified to better suit the ball screw-nut. The effect of the extra axial displacement caused by unrigid connection between the screw and its supporting housing is more reasonably considered.

The Frenet-Serret coordinate system, which describes the motion of one of the spheres, is introduced to better understand the friction and inside compliance effect of screw-nut mechanism. The origin is located in the considered sphere center; the  $x_2$  axis is tangent to the helical path; the  $y_2$  axis points towards the screw axis and  $z_2$  is the normal axis. As shown in Fig. 3, the compliance effect between components can be considered on the normal plane  $y_2\omega_2z_2$  (perpendicular to the helical path). The slip friction force occurs along the  $x_2$  axis (tangent to helical path).<sup>23</sup>

#### 3.1.1. Compliance effect

Referring to Fig. 3, the normal contact force  $F_{bs}$  between screw groove and ball, as well as normal contact force  $F_{nb}$  between ball and nut groove can be separately derived as

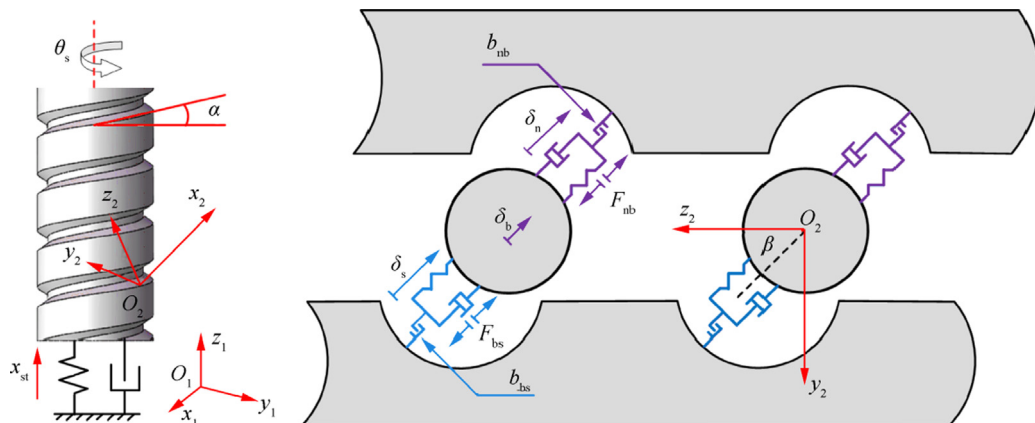


**Fig. 3** Contact model of Screw-nut mechanism.

$$\begin{cases} F_{bs} = (k_{sn}\Delta x_{bs} + d_{sn}\Delta \dot{x}_{bs})|f_1| \\ F_{nb} = (k_{sn}\Delta x_{nb} + d_{sn}\Delta \dot{x}_{nb})|f_2| \\ \Delta x_{bs} = \delta_b - \delta_s - f_1 b_{bs} \\ \Delta x_{nb} = \delta_n - \delta_b - f_2 b_{nb} \end{cases} \quad (1)$$

where  $\delta_s$ ,  $\delta_b$  and  $\delta_n$  are respective displacements along normal direction;  $k_{sn}$  and  $d_{sn}$  are contact stiffness and damper rating, respectively;  $b_{bs}$  and  $b_{nb}$  are respective backlashes.  $f_1$  and  $f_2$  are introduced for auxiliary calculations. In the absence of active contacts, i.e., the backlashes are not recovered completely,  $f_1$  and  $f_2$  are forced to zero. Otherwise,  $f_1$  and  $f_2$  equal to the return values of sign function, where the variable inputs are their corresponding contact forces.

The equilibrium equation of the sphere along the normal direction can be written as

$$m_b \ddot{\delta}_b = F_{nb} - F_{bs} \quad (2)$$

where  $m_b$  is the equivalent translating mass of the recirculating balls.

$\delta_s$  and  $\delta_n$  can be expressed as

$$\begin{cases} \delta_n = x_n \cos \alpha \sin \beta \\ \delta_s = \theta_s R_e \sin \alpha \sin \beta + x_{st} \cos \alpha \sin \beta \end{cases} \quad (3)$$

where  $\theta_s$  and  $x_n$  refer to screw angular displacement and nut translation displacement;  $x_{st}$  reflects the extra axial displacement (Fig. 3) caused by compliance effect due to mechanical load path and it can be imposed to zero if the mechanical transmission is assumed as infinitely rigid;  $\alpha$  and  $\beta$  are helix angle and contact angle, respectively.  $R_e$  is defined as the circle radius of the contact point of screw groove and ball.

And the speeds along the  $t$  axis at the contact points for screw and nut can be derived as:

$$\begin{cases} v_{bs} = \dot{\theta}_s R_s \cos \alpha + \dot{x}_{st} \sin \alpha \\ v_{nb} = -\dot{x}_n \sin \alpha \end{cases} \quad (4)$$

#### 3.1.2. Friction effect

The friction force  $F_{fs}$  between the screw and ball, as well as friction force  $F_{fn}$  between the nut and ball, is considered as a coulomb friction model for two considerations. First, adopting a more realistic friction model would require more parameters to be acquired; Secondly, since the no-back friction is the dominant friction source, utilizing the simple coulomb friction model will barely sacrifice the system-level precision:

$$\begin{cases} F_{fs} = f_{cl} F_{bs} \\ F_{fn} = f_{cl} F_{nb} \end{cases} \quad (5)$$

where  $f_{cl}$  is denoted as the coulomb friction factor;  $F_{bs}$  and  $F_{nb}$  are the contact forces.

Consequently, assuming that the balls do not slip, the screw torque  $T_s$ , axial force transmitted by screw shaft  $F_{st}$  and the axial output force on nut  $F_n$ , can be respectively determined as:

$$\begin{cases} T_s = (F_{bs} \sin \alpha \sin \beta + F_{fs} \cos \alpha) R_c \\ F_{st} = -F_{bs} \cos \alpha \sin \beta + F_{fs} \sin \alpha \\ F_n = F_{nb} \cos \alpha \sin \beta - F_{fn} \sin \alpha \end{cases} \quad (6)$$

With respect to another screw–nut (secondary nut) mechanism, the transformation from rotary motion to linear motion is directly implemented by thread engagement (without recirculating balls). Therefore, its model can be easily obtained by combining the modelling principle in early researches<sup>22</sup> and the modifications in this paper.

### 3.2. Mechanical load path

The mechanical load path enables the transmission of the external axial load to the airframe. Reproducing its realistic elastic behavior is particularly necessary, because compliance effect significantly impacts the dynamic performance and the service life. Furtherly, the dual load path, used for mechanical redundancy, should be involved for fail-safe mode verification.

The respective components of mechanical load path are illustrated in Fig. 4 (a). The rotary motion to translation motion transform is accomplished via ball screw and ball nut. A secondary nut with inverted thread and the same lead is utilized as a backup to the primary load path ball nut. The secondary load path works as mechanical redundancy, by sharing the extern load in the event of primary load path failure. In normal operation, the initial assembly clearances, which are annotated with texts in Fig. 4 (a), guarantee that none force can be transmitted via the secondary load path.

The flight control surface is attached to actuator through the lower gimbal assembly. The control surface load is transmitted via the screw-nut mechanism and exerts an axial load to the screw. This axial load is eventually supported by the screw housing and rear attachment components belonging to mechanical load path.

The working principle diagram of mechanical load path is illustrated in Fig. 4 (b). The power input is the torque and screw shaft velocity  $\omega_s$  from gearbox, whereas the power output is the trimming speed of THS and drive force to balance the aerodynamic force  $F_L$ . The torque input balances several effects: inertia torque effect  $J_s$ , friction torque loss from the no-back mechanism, screw driving torque  $T_s$ .

As illustrated in Fig. 4 (b), since the separate modelling of each individual compliance effect between components is difficult, modelling has been reasonably simplified and conducted at the global level, by merging the whole compliance effects into lumped stiffness and damping inside the screw housing and rear attachment components. Based on the geometry investigation of no-back mechanism components in Fig. 4 (a), the tensile or compressive force exerted on screw can be transmitted via two parallel paths. Each path shows its own compliance. The first one corresponds to a preload disk spring to ensure both upper and lower no-back mechanism components are tightly engaged, whereas the other corresponds to a spring-damper element with purposely reserved backlash. For convenience, backlash or preload effect can be defined by a proposed single parameter  $x_0$  with positive or negative signs, respectively.<sup>24</sup> For the no-back mechanism with bilateral backlash  $b_{pb}$  and preload  $-b_{ds}$ , the total transmitted force  $F_{st}$  from screw to airframe is

$$F_{st} = F_{b,l} + F_{b,u} = \begin{cases} k_{p,u}(x_{st} - b_{pb}) + 2k_{ds}x_{st} + d_{pb}x_{st} & x_{st} \geq b_{pb} \\ 2k_{ds}x_{st} & -b_{pb} < x_{st} < b_{pb} \\ k_{p,l}(x_{st} + b_{pb}) + 2k_{ds}x_{st} + d_{pb}x_{st} & x_{st} \leq -b_{pb} \end{cases} \quad (7)$$

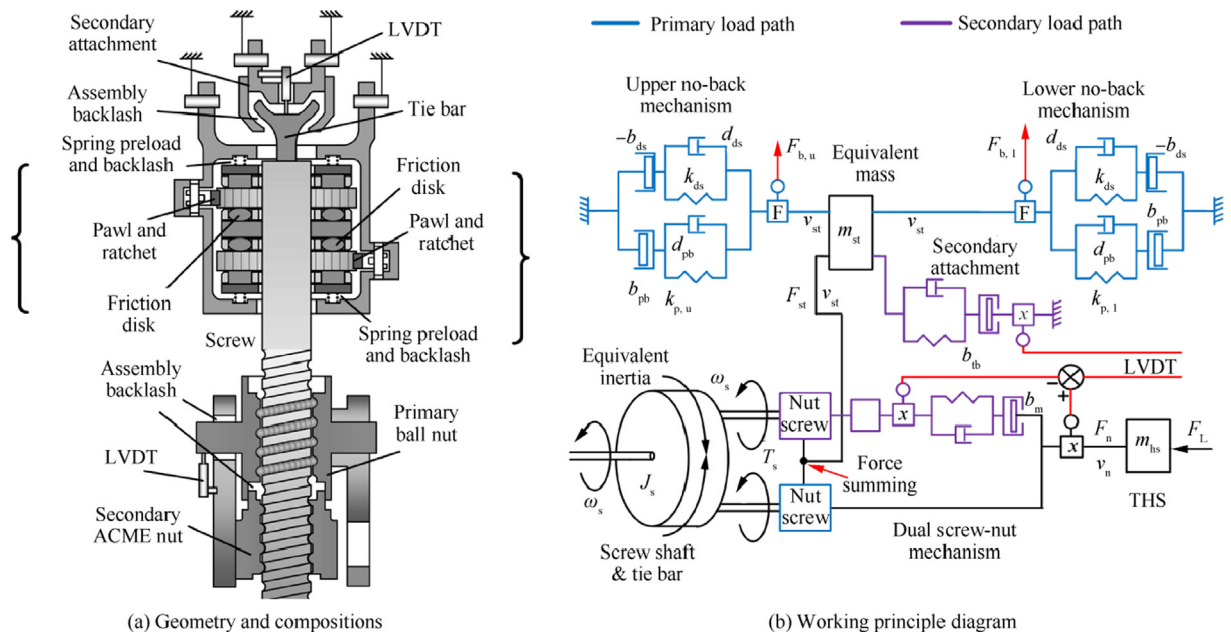


Fig. 4 Working principle analysis of mechanical load path.

where  $x_{st}$  is the additional linear displacement caused by the compliance effect of load path between screw housing and rear attachment components and airframe;  $k_{p,l}$ ,  $k_{p,u}$  and  $k_{ds}$  are equivalent no-back stiffness and stiffness of preload disk spring;  $d_{pb}$  is the contact damper rating;  $F_{b,l}$  and  $F_{b,u}$  stand for the transmitted force by lower and upper no-back mechanism, respectively.

The mechanical load path redundancy is relying on the secondary ACME nut and the tie bar. Meanwhile, the tie bar, which can transmit the axial loads internally to the THS screw, are axially connected by thread and circumferentially connected by spline with the screw shaft. That is why the tie bar will not be modelled separately. The screw and tie bar are treated as a whole by using a combined mass or inertia element. Similarly, the compliance effects considering backlash effects between primary load path and secondary load path components are referred as spring-damper elements with initial clearances  $b_{tb}$  and  $b_{rn}$ . Thanks to the LVDT sensors respectively mounted on secondary attachment and secondary nut assembly, the EMCU can detect the clearances variations ( $b_{tb}$  and  $b_{rn}$ ) between dual load paths and consequently perform fault monitoring to primary load path.

### 3.3. No-back mechanism

When the load force becomes aiding and in the absence of actuation torque, the screw is braked against the THSA housing, otherwise the no-back does not (functionally) oppose any torque to the rotation the shaft. This is achieved with ratchet wheels, which are enabled by pawls given the direction of the axial load and trim direction. The friction torque and the circumferential clearance between pawl and ratchet wheel are worth given attention, because they directly affect the actuator uncontrolled displacement and compliance effect of the no-back mechanism.

#### 3.3.1. Overall analysis of modelling principle

As shown in Fig. 4, The complete no-back mechanism is composed of upper no-back mechanism assembly, lower no-back mechanism assembly and no-back housing assembly. To realize bidirectional irreversibility function, the no-back pawls block the rotation of their respective ratchet wheel relative to the actuator body, each operating for a different rotation direction.

However, solely relying on the bidirectional ratchet and pawl mechanisms, the THS position cannot be adjusted with the pilot/autopilot command. Consequently, to overcome this problem, the friction disks are utilized and inserted between

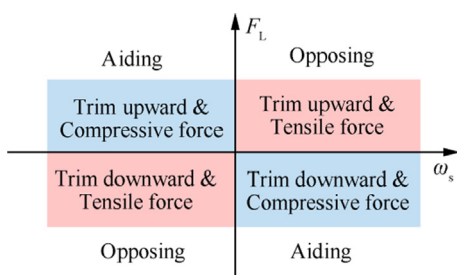


**Fig. 5** Complete working quadrants of THSA.

the screw flange and ratchet wheel. As shown in Fig. 5, the complete working quadrants of THSA are included to provide a working principle difference whether the load is aiding or opposing. The positive sign of velocity and load are respectively defined as counter-clockwise (trim upward) and tensile force (downward). For simplification, some reasonable hypotheses are proposed:

- 1) The friction from friction disk is proportional to the contact force, and the friction coefficient is constant;
- 2) The friction magnitude caused by the ratchet's free-wheeling rotation is neglected.

There exist two potential operation states for the pawl and ratchet mechanism, i.e., blocked or freewheeling. At the 'freewheeling' state, the pawl offers rarely no resistance to the ratchet's rotation, which implies that the ratchet, friction disk and the screw flange are bonded by static friction torque with small magnitude. At the 'blocked' state, the ratchet is forced to be stationary. And the stiction friction may be overridden and transformed into sliding friction, if the screw is continuously driven in rotation relative to the stationary ratchet. Meanwhile, except for the operation state, the contact force between no-back components significantly influences the friction. Two preload disk springs are symmetrically utilized to make both upper and lower no-back mechanism components tightly engaged. The stiction friction resulting from this preload force can ensure a steadier surface position under light loads. The contact force magnitude of the no-back mechanism locate opposite to the load direction is determined by the residual preload force. However, as shown in Fig. 6 if the load continuously increases and becomes larger than twice the preload force  $F_p$ , the residual spring preload force will gradually decrease and finally disappear.

To qualitatively introduce the detailed working principles, the crucial components are graphically presented under different trim directions by exerting bidirectional THS load  $F_L$ . Firstly, the actuator is considered inactive under compressive load, as well as the angular velocity is zero ( $\omega_s = 0$ ). As shown in Fig. 7 (a), the upper ratchet wheel is blocked by its pawl to avoid the screw revolving due to the axial force exerted by the load on the nut, whereas the lower ratchet wheel is permitted freewheeling. The load torque  $T_L$  generated on the screw by the THS is balanced by the stiction friction torque produced by the upper friction disks. Fig. 8 (a) and Fig. 9 (a) illustrate the individual friction variations and operation states versus the compressive load, when the THSA is inactive.

For one and the same direction of load force, the actuator is active and must move the nut upward corresponding to a pos-

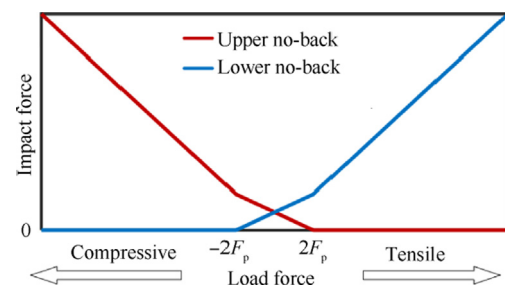


**Fig. 6** Contact force magnitude variation versus load force.

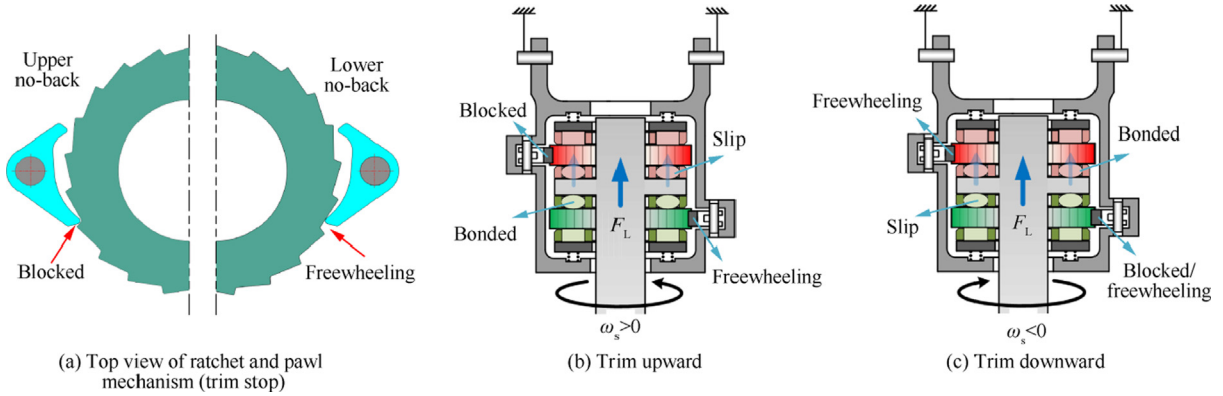


Fig. 7 No-back mechanism working principle analysis under compressive force.

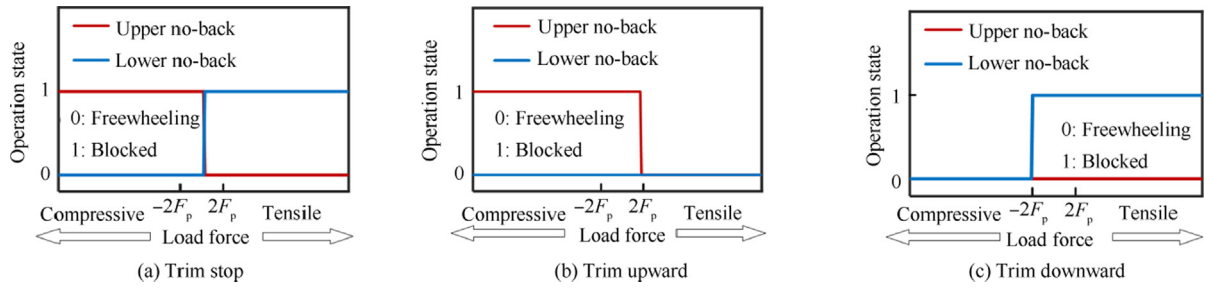


Fig. 8 No-back operation states at different trim directions.

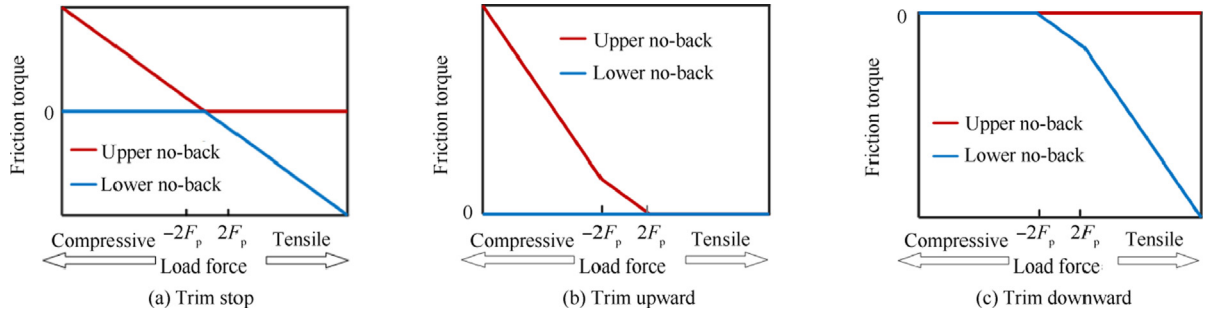


Fig. 9 Individual friction torque variation versus load at different trim directions.

itive sign of  $\omega_s$  in Fig. 7 (b). Therefore, the movement has the same direction as back-driven direction caused by the aerodynamic load force: the load is aiding. The actuator must develop a driving torque on the screw to override the breakaway friction torque produced from the upper friction disk. However, essentially no friction torque is developed from lower brake mechanism, since the lower ratchet wheel is permitted free-wheeling in current direction. Fig. 8 (b) and Fig. 9 (b) illustrate the individual friction variations and operation states versus the compressive load, when THSA trims upward.

On the contrary, if the actuator must move the nut downward corresponding to a negative sign of screw velocity  $\omega_s$  in Fig. 7 (c) (the load is opposing), both the upper and lower brakes functionally reverse their modes of operation. The upper ratchet is permitted freewheeling, whereas the lower ratchet is supposed to be blocked, instead. Consequently,

essentially no friction torque is developed from upper brake mechanism. And a sliding friction torque is generated from the lower friction disk, because the residual spring preload force still guarantee the axial tight engagement of the lower brake mechanism components. However, as addressed above in Fig. 6, the compressive load with sufficiently large amplitude will eliminate the residual spring preload force. Therefore, the lower ratchet is able to rotate freewheeling again. Fig. 8 (c) and Fig. 9 (c) illustrate the individual friction variations and operation states versus the compressive load, when the THSA trims downward.

The above principle analysis is made when the load is compressive. For the opposite direction of load force, i.e., tensile force, the working principle analysis process can be conducted similarly, and the conclusions are also collected in Table 1, Fig. 8 and Fig. 9. Combining the above investigation, the fric-

**Table 1** No-back mechanism working principle under tensile force.

Direction	Trim stop		Trim upward		Trim downward	
	Upper	Lower	Upper	Lower	Upper	Lower
No-back mechanism	—	—	Upper	Lower	Upper	Lower
Load characteristic	—	—	Opposing load	—	Aiding load	—
Operation state of ratchet wheel and pawl	Blocked	Freewheeling	Freewheeling/ Blocked*	Freewheeling	Freewheeling	Blocked
Operation state of ratchet wheel and friction disk	Bonded by friction	—	Relative slip	Bonded by friction	Bonded by friction	Relative slip

\*: ‘Blocked’ with  $F_L > 2F_p$  condition, ‘Freewheeling’ with otherwise conditions.

tion characteristic of no-back mechanism can be summarized as follows:

- 1) The operation states of both pawl and ratchet mechanisms are completely dependent on the force applied by the driven load, when the actuator is inactive; When the actuator is active and trims for pitch control, both operation states are determined by the rotation directions of screw shaft, if the residual preload force still exists. However, if the actuator works under opposing load and the load force is larger enough to eliminate the preload force, both upper and lower ratchet operate at freewheeling state. It is observed that the slopes between the friction torque versus load force experience a sudden variation, which is resulting from the disappear of one-side preload force.
- 2) By further consideration on Fig. 9, the relationship between total no-back friction, screw velocity and load force can be obtained and graphically shown in Fig. 10. It is noted that the no-back friction under specific trim direction and different load directions can be either load dependent or hold to the small tare value. The reason about this special phenomenon is relevant to no-back operation states determined by trim direction, and load distributions determined by load direction and amplitude.
- 3) According to the actuator work quadrants in Fig. 5, the total friction torque versus the load performance is shown in Fig. 10 (c), It is obvious that the total friction torque in aiding situation shows much bigger magnitude than that in opposing situation, which can be explained by the contact force differences in Fig. 6. Consequently,

with a relatively large load force, the actuator may require more motor current to overcome the friction torque on aiding load condition.

### 3.3.2. Compliance and friction effect analysis

As addressed above, each ratchet wheel operates in two modes, i.e., freewheeling or blocked. For convenience, the screw velocity direction permitting the ratchet wheel freewheeling is defined as opposing direction, whereas the velocity direction causing the ratchet wheel blocked by its corresponding pawl is defined as aiding direction. When the screw velocity switches into opposite direction, functionally the mode of operation of each ratchet wheel reverses. However, due to the existence of circumferential angle between adjacent ratchet teeth, a circumferential clearance must be eliminated, before the ratchet wheel and pawl achieve active contact. More importantly, this circumferential clearance is dependent on the immediate position of ratchet wheel. Attributing to strain gauges arranged on the housing of pawls, strain signal will occur a sudden variation, when the ratchet wheel is blocked by the pawl. Consequently, the immediate circumferential clearance can be calculated according to the screw angular displacement difference from the velocity direction inverse clock to the block occurrence clock.

The contact torques  $T_{c,u}$  and  $T_{c,l}$  can be derived by considering the compliance effect with backlash:

$$\begin{cases} T_{c,u} = \left( k_p(\theta_{r,u} + \theta_{b,u}) + d_p \dot{\theta}_{r,u} \right) f_{b,u} \\ T_{c,l} = \left( k_p(\theta_{r,l} - \theta_{b,l}) + d_p \dot{\theta}_{r,l} \right) f_{b,l} \end{cases} \quad (8)$$

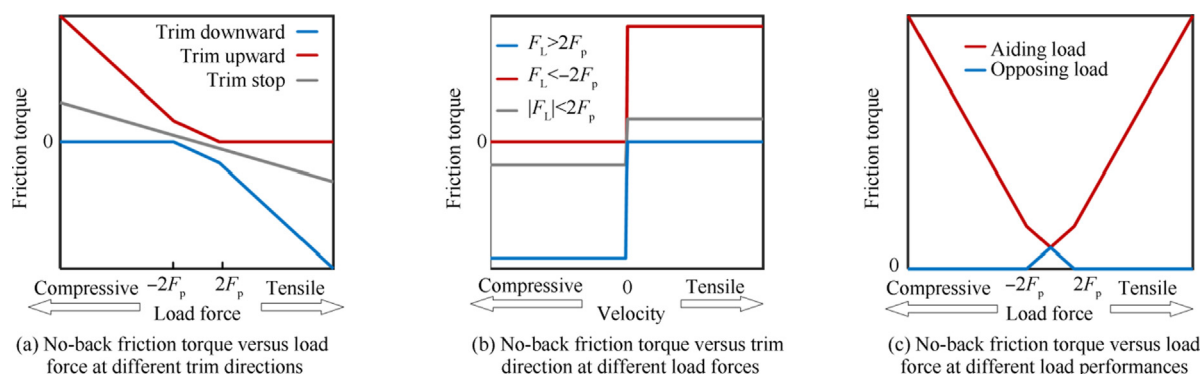


**Fig. 10** Total no-back friction torque versus load magnitude, velocity and load performance.

where  $\theta_{r,u}$  and  $\theta_{r,l}$  refer to respective angular displacements for upper and lower no-back mechanism, after the screw velocity switches into aiding direction;  $f_{b,u}$  and  $f_{b,l}$  are imposed to 1, when active contact occurs:

$$f_{b,u} = \begin{cases} 1 & \theta_{r,u} + \theta_{b,u} < 0 \\ 0 & \theta_{r,u} + \theta_{b,u} \geq 0 \end{cases}, f_{b,l} = \begin{cases} 1 & \theta_{r,l} - \theta_{b,l} > 0 \\ 0 & \theta_{r,l} - \theta_{b,l} \leq 0 \end{cases} \quad (9)$$

The friction loss in the no-back mechanism is a complex phenomenon that is highly dependent on velocity, external load and temperature.<sup>13</sup> The suggested model of friction for no-back mechanism is:

$$T_f = [\mu_c + (\mu_s - \mu_c)e^{-(\omega_s/\omega_{st})^2}]|F|\text{sgn}(\omega_s) + f_s\omega_s \quad (10)$$

where  $\mu_s$  and  $\mu_c$  are the stick and coulomb friction coefficient, respectively;  $\omega_{st}$  is the stribbeck reference velocity;  $F$  is normal contact force;  $f_s$  is the viscous friction coefficient. It is emphasized that this proposed model includes the contact force transmitted from the external load, this significant effect being often ignored in the modelling of mechanical transmission devices. The subscripts  $i$  ( $i = u, l$ ) distinguish upper and lower no-back mechanism.

### 3.4. Modelling of fault injection and monitoring

Simulating the response to failure of THSA is mandatory for flight control systems to assess fault tolerant and health monitoring functions. Combining the mainly feared events of an EMA are summarized by Balaban,<sup>25</sup> the focused faults here includes load path failure and jamming fault, whereas the failure of the gears, motors, drives and controllers are not concerned here.

The THSA utilizes redundant load paths configured as active/standby solution, and normal and backups flows of axial force are shown in Fig. 4 (a). The primary load path failure can be injected by inserting backlash between the components of the load path, such as upper gimbal assembly and airframe. In addition, the respective LVDT sensors have been arranged properly to monitor the clearance variations between dual load paths to serve the fault detection, which can be achieved by comparing the actual clearance variations to a given threshold in normal operation.

According to the location in the mechanical transmission, jamming fault can be classified as ‘internal or ‘external’, i.e. inside THSA or in the attachments to the control surface, respectively.<sup>15</sup> The former category can be represented via a typical jamming fault occurring inside screw-nut mechanism and can be simulated by applying a step increase of friction force.<sup>13</sup> The latter category can be injected by mechanical locking the control surface position. The jamming fault monitoring is implemented via the compassion of different trim speed feedbacks acquired from RVDT and motor position sensor respectively. When the screw-nut mechanism or control surface encounters a jamming fault, the great load torque causes the relative slip occurrence inside the torque limiter, which generates a great difference between these two speed feedbacks. If the time duration, where the actual speed difference constantly stays larger than permitted threshold, exceeds the time threshold, this fault can be detected by EMCU. Previous researches have suggested detailed diagnosis methods for motor faults (short circuit, open circuit, sensor faults).<sup>26,27</sup> Meanwhile, it

is important to note that no particular attention is paid to detailed fault diagnosis methods<sup>28,29</sup> and fault tolerance algorithm,<sup>30</sup> which have been well documented.

## 4. Virtual prototype and model implementation

The former sections have presented the THSA model architecture and the nonlinear multidisciplinary effects. Therefore, analytical studies are no longer adequate and numerical simulation becomes mandatory. A virtual prototype of THSA system is established in the multi-domain system-level simulation environment, AMESim (Fig. 11 and Fig. 12). It is noted that the contribution of this paper is to convert the mechanical design to the lumped parameters modelling by combining various effects (functional and parasitic) in the most relevant way. That is why the implementation process from the mathematic model to the prototype will not be detailed presented. The model implementation methods of MCE or MBA in AMESim can be easily found from the previous literature.<sup>13</sup> For convenience, the mechanical transmission parts are split into several modules based on the energy flow relationship in Fig. 2, including gearbox, no-back mechanism, mechanical load path and screw-nut mechanism. The mainly utilized parameters for the following simulations are displayed in Table 2. The parameters to evaluate the nonlinear compliance effect and friction effect for mechanical load path and no-back mechanism have been identified from relevant experiments in author’s previous work.<sup>31</sup>

## 5. Simulation and experimental results

As shown in Fig. 13, a real test rig for THSA has been built for experimental verification. This test rig enables the THSA to be closed loop controlled in speed. In addition, an electromechanical load generator is used to apply a force on the dummy THSA, which is representative of the airload acting on the THS, as a function of the flight conditions. And an inertia block is placed at the end of the lever to represent the THS inertia. For testing, strain gauges are placed at different locations of the THSA housing, in order to measure the mechanical stress. The trim speed control and load control are executed by dummy controllers, based on the command signals from the operation terminal and sensor data. All the experimental results are available in the operation terminal for operators.

When the actuator is inactive, the authors’ previous work has verified the correct switching of state of the ratchet and pawl with constant speed command and varying external load input, and demonstrated the effect on system performance caused by no-back friction.<sup>31</sup> Here, the more comprehensive validation of modelling principle analysis is conducted. The influence of nonlinearities on system performance will be focused to show how nonlinear effects affect the THSA dynamic performance.

To synthetically and quantitatively compare the dynamic performance differences of simulation and experimental results, the following performance indexes are referred, including mean motor currents under opposing and aiding conditions ( $I_{mo}$ ,  $I_{ma}$ ), maximum tracking error of trim speed ( $E_{vmax}$ ) and mean tracking error of trim speed ( $E_{vmean}$ ). In addition, when operation states of lower or upper ratchet and pawl switches

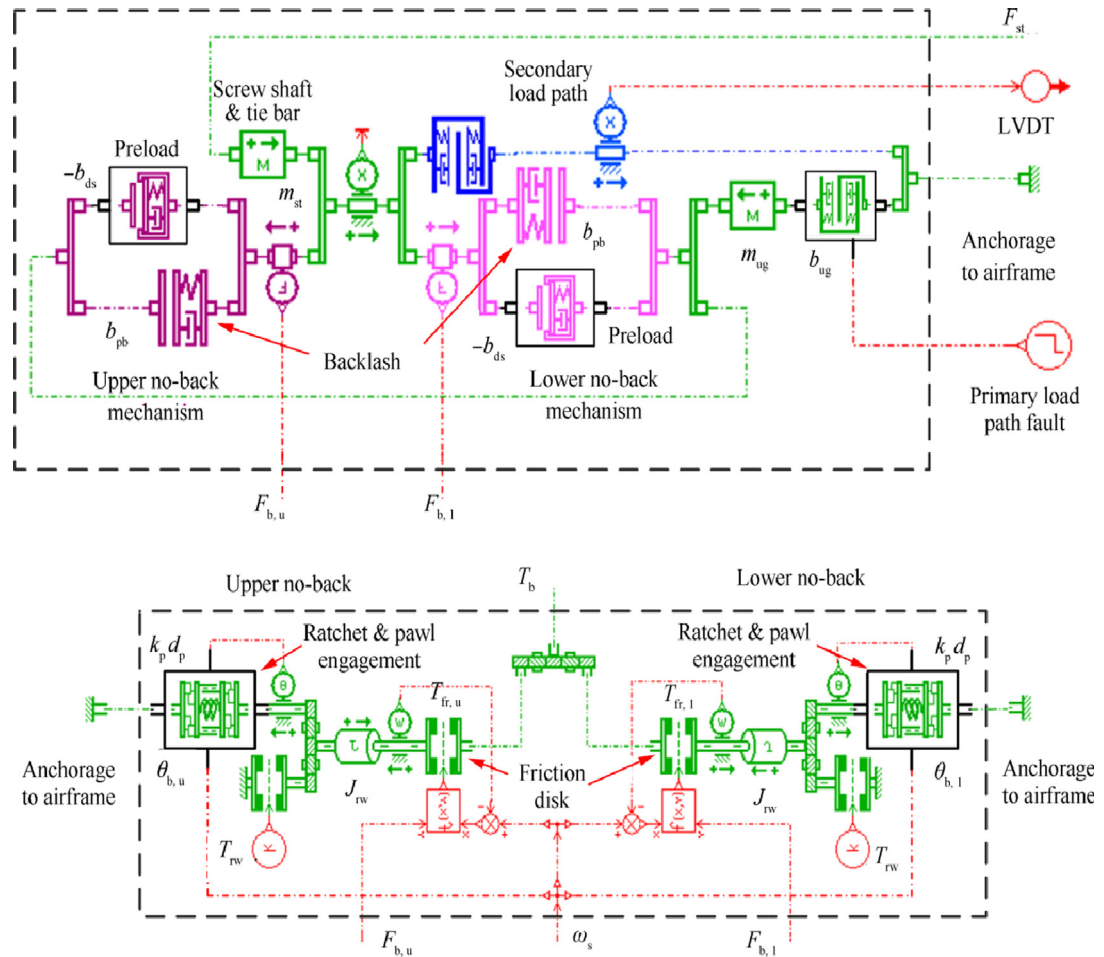


**Fig. 11** Virtual prototype of mechanical load path module and no-back mechanism.

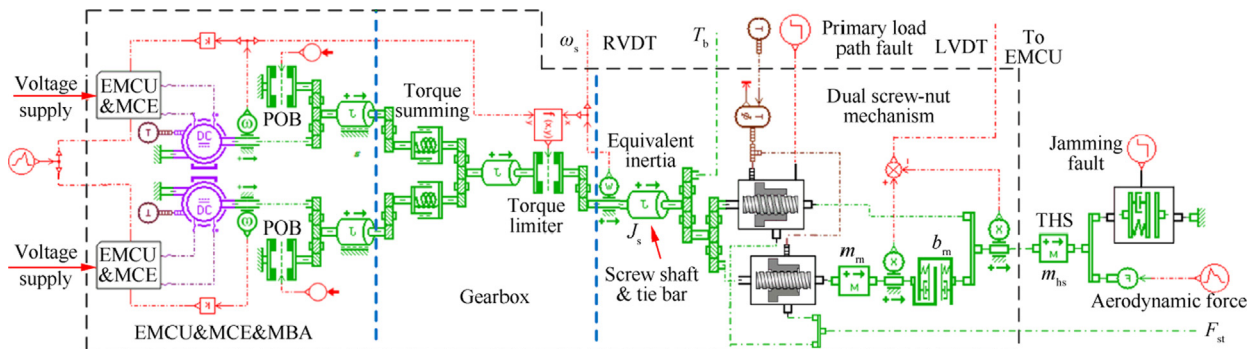


**Fig. 12** Virtual prototype of gearbox, screw-nut mechanism and control surface.

from ‘blocked’ to ‘freewheeling’, the time clocks are respectively denoted as  $t_{bf,1}$  and  $t_{bf,u}$ ;  $t_{fb,1}$  and  $t_{fb,u}$  represent the opposite switching clocks of operation states.

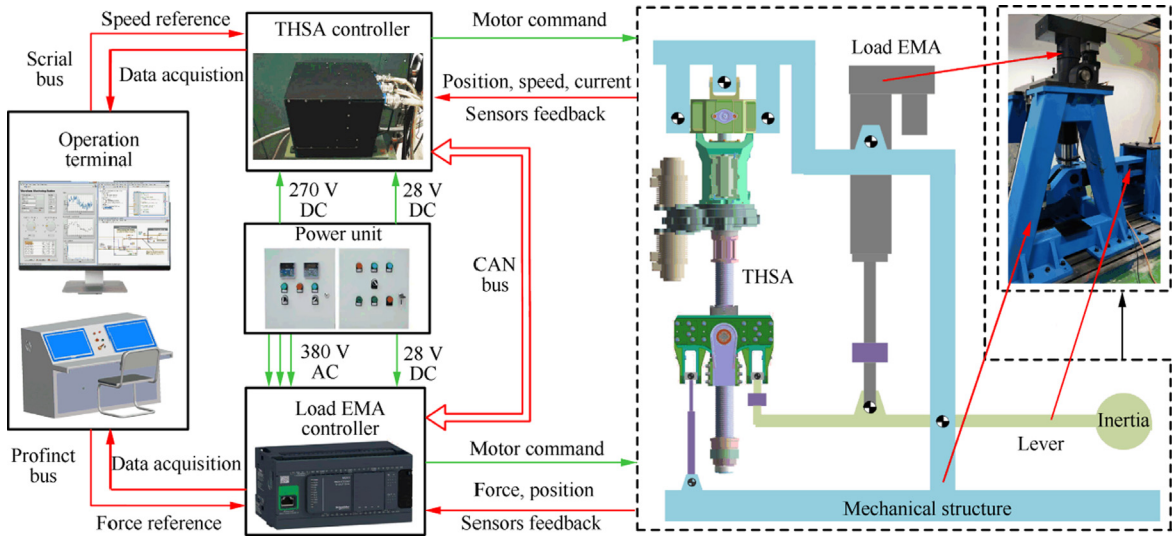
### 5.1. Response to triangular aerodynamic force

First, a negative trapezoidal trim speed command with an amplitude 15 mm/s and acceleration 30 mm/s<sup>2</sup> is applied at time 1 s. Simultaneously, a force demand from the load gener-

ator is triangular, with an amplitude of 29 kN and period of 15 s, as shown in Fig. 14 (a). It is noted that the realized force is not the exact triangle demand because of the bounded dynamic performance of the load generator. The reason for choosing this excitation is to validate the no-back friction differences under different load performances (aiding or opposing). Another is to make the mechanical load path experience different stiffness values, which further verifies how the compliance effect between screw and its housing influ-

**Table 2** Key parameters for virtual prototype.

Symbol	Value	Unit	Symbol	Value	Unit	Symbol	Value	Unit
$J_m$	$1.8 \times 10^{-4}$	$\text{kg}\cdot\text{m}^2$	$k_t$	0.38	$\text{N}\cdot\text{m}\cdot\text{A}^{-1}$	$R_s$	1.23	$\Omega$
$L_s$	2.25	mH	$T_{POB}$	2.5	N·m	$f_v$	$3.0 \times 10^{-4}$	$\text{N}\cdot\text{m}\cdot\text{rad}^{-1}\cdot\text{s}$
$I_{max}$	15	A	$U_{dc}$	270	V	$i$	65.61	–
$T_n$	2.0	N·m	$k_g$	500	$\text{N}\cdot\text{m}\cdot\text{deg}^{-1}$	$d_g$	50	$\text{N}\cdot\text{m}\cdot\text{rad}^{-1}\cdot\text{s}$
$F_p$	500	N	$J_{rw}$	$3.0 \times 10^{-3}$	$\text{kg}\cdot\text{m}^2$	$T_{rw}$	0.5	N·m
$k_p$	$1\text{e}^4$	$\text{N}\cdot\text{m}\cdot\text{deg}^{-1}$	$d_p$	850	$\text{N}\cdot\text{m}\cdot\text{rad}^{-1}\cdot\text{s}$	$\omega_{st}$	15	$\text{r}\cdot\text{min}^{-1}$
$\mu_s$	$7.0 \times 10^{-3}$	m	$\mu_c$	$4.5 \times 10^{-3}$	m	$l_s$	12	mm
$R_e$	55	mm	$f_c$	$7.0 \times 10^{-3}$		$\beta$	45	deg
$m_{hs}$	350	kg	$m_{st}$	15	kg	$m_{ug}$	30	kg
$m_b$	1.5	kg	$J_s$	0.1	$\text{kg}\cdot\text{m}^2$	$k_{ds}$	$1.5 \times 10^6$	$\text{N}\cdot\text{m}^{-1}$
$k_{sn}$	$5 \times 10^8$	$\text{N}\cdot\text{m}^{-1}$	$d_{sn}$	$1 \times 10^6$	$\text{N}\cdot\text{m}^{-1}\cdot\text{s}$	$d_{pb}$	$1.0 \times 10^6$	$\text{N}\cdot\text{m}^{-1}\cdot\text{s}$
$k_{p,u}$	$5.3 \times 10^7$	$\text{N}\cdot\text{m}^{-1}$	$k_{p,1}$	$6.7 \times 10^7$	$\text{N}\cdot\text{m}^{-1}$	$b_{pb}$	0.75	mm
$b_{rn}$	2.5	mm	$b_{tb}$	2.5	mm			

**Fig. 13** Test rig for THSA.

ence the surface speed based on the modified screw-nut model. And the results of the performance indexes are shown in Table 3.

The clearance variations of the mechanical load path, as well as the transmitted force of each no-back mechanism versus the external load are depicted in Fig. 14 (d), where the negative values imply that the backlash has been recovered, i.e., under active contacts. When backlash exists inside upper or lower no-back mechanism, the magnitude of the normal contact force comes from the residual preload force. And this magnitude will translate into the sum of preload force and load force with the backlash gap closed.

The operation states of both pawl and ratchet mechanism are shown in Fig. 14 (b). When the actuator trims downward under aiding load, the operation states of lower and upper pawl and ratchet mechanism consistently and respectively maintain blocked and freewheeling, which matches the no-back mechanism working principle in section 3. However, when the actuator trims downward continuously under opposing load, the increasing load amplitude causes that the residual

preload force disappears for lower no-back mechanism. Hence, the operation mode of lower pawl and ratchet mechanism transforms into freewheeling in the absence of contact force. The operation modes of pawl and ratchet mechanism make the total friction torque mainly coming from the slipping friction generated from the lower friction disk in Fig. 14 (c). Subsequently, as shown in Fig. 14 (d), the normal contact force variation of lower no-back mechanism causes the huge friction torque differences under opposing or aiding conditions, which can be verified by the simulation and experimental results of the motor phase current in Fig. 14 (c). From Table 3, it can be observed that the opposing current amplitude is about 73% of aiding current amplitude.

The impact of mechanical load path compliance effect on system performance is established by comparing the surface speed responses of models with different complexities and experimental results. If the backlash effect is introduced in the model, the structural stiffness is mainly dependent on the disk spring, when the external load amplitude is not large enough to eliminate the initial clearance. Compared to simula-

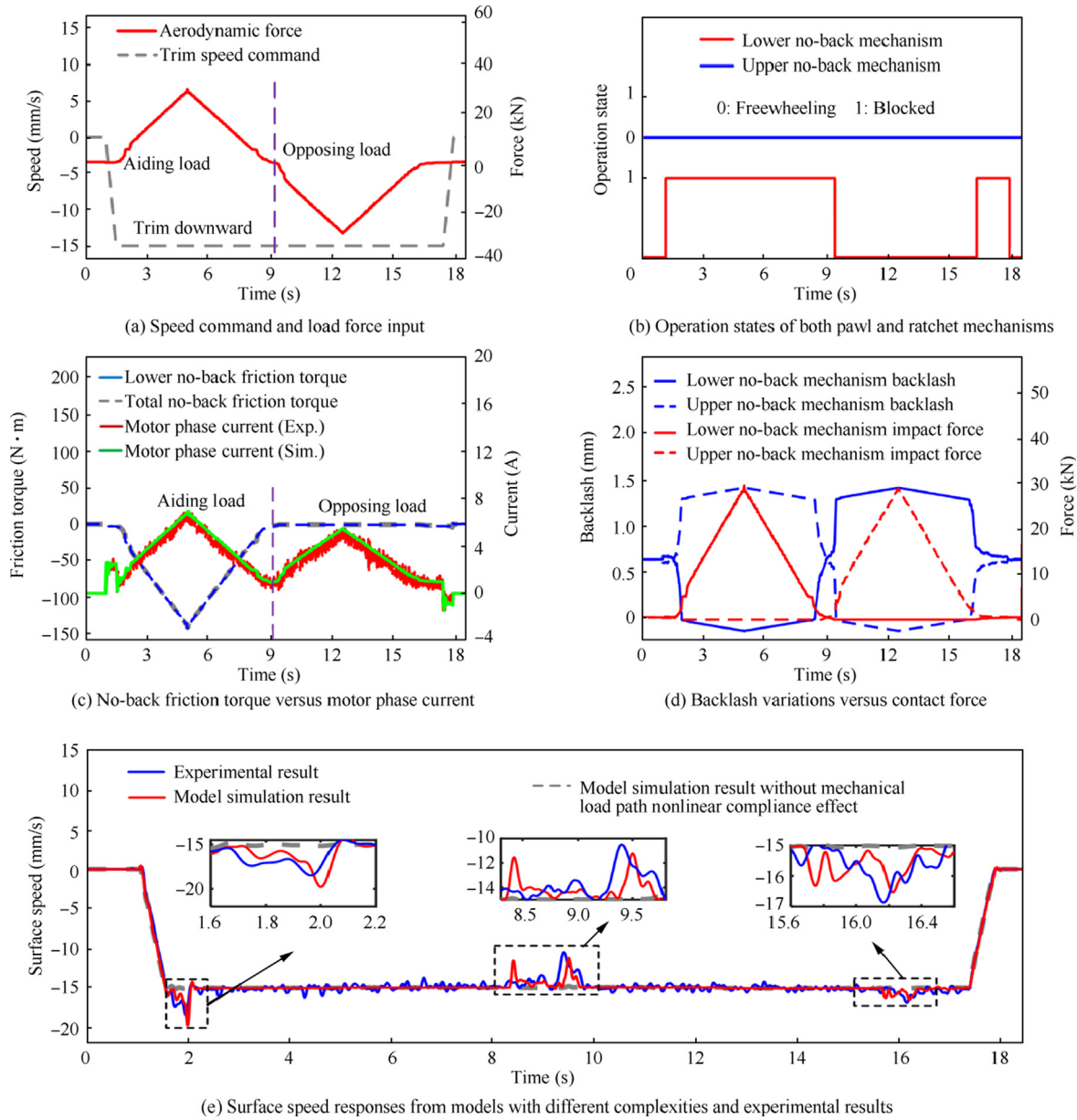


**Fig. 14** Simulation and experimental results under triangular aerodynamic load.

**Table 3** Simulation and experimental results of dynamic performance under triangular aerodynamic load.

Item	$t_{bf, 1}$ (s)	$t_{bf, u}$ (s)	$t_{fb, 1}$ (s)	$t_{fb, u}$ (s)	$I_{mo}$ (A)	$I_{ma}$ (A)	$E_{vmax}$ (%)	$E_{vmean}$ (%)
Model simulation results without mechanical load path nonlinear compliance effect	—	—	—	—	—	—	14.8	0.00
Model simulation results	9.360	—	1.116	—	3.41	4.35	31.8	0.00
Experimental results	—	—	—	—	2.75	3.75	29.9	0.19

tion result with ideal structural stiffness, from equation and, this poor stiffness causes an additional linear displacement/speed to the screw-nut mechanism and leads to the oscillation of surface speed in Fig. 14 (e). From Table 3, the maximum following error increases from 15% to about 30%. According to equation, when the load force continues increasing, the

backlash is gradually eliminated and the structural stiffness returns to normal. That is why responses from both models and experimental results are globally consistent during these phases. Since clearances from upper and lower no-back mechanism are unilateral and symmetrical about the screw flange, it

is noted that these two clearances share the opposite variation trends under the same load direction in Fig. 14 (d).

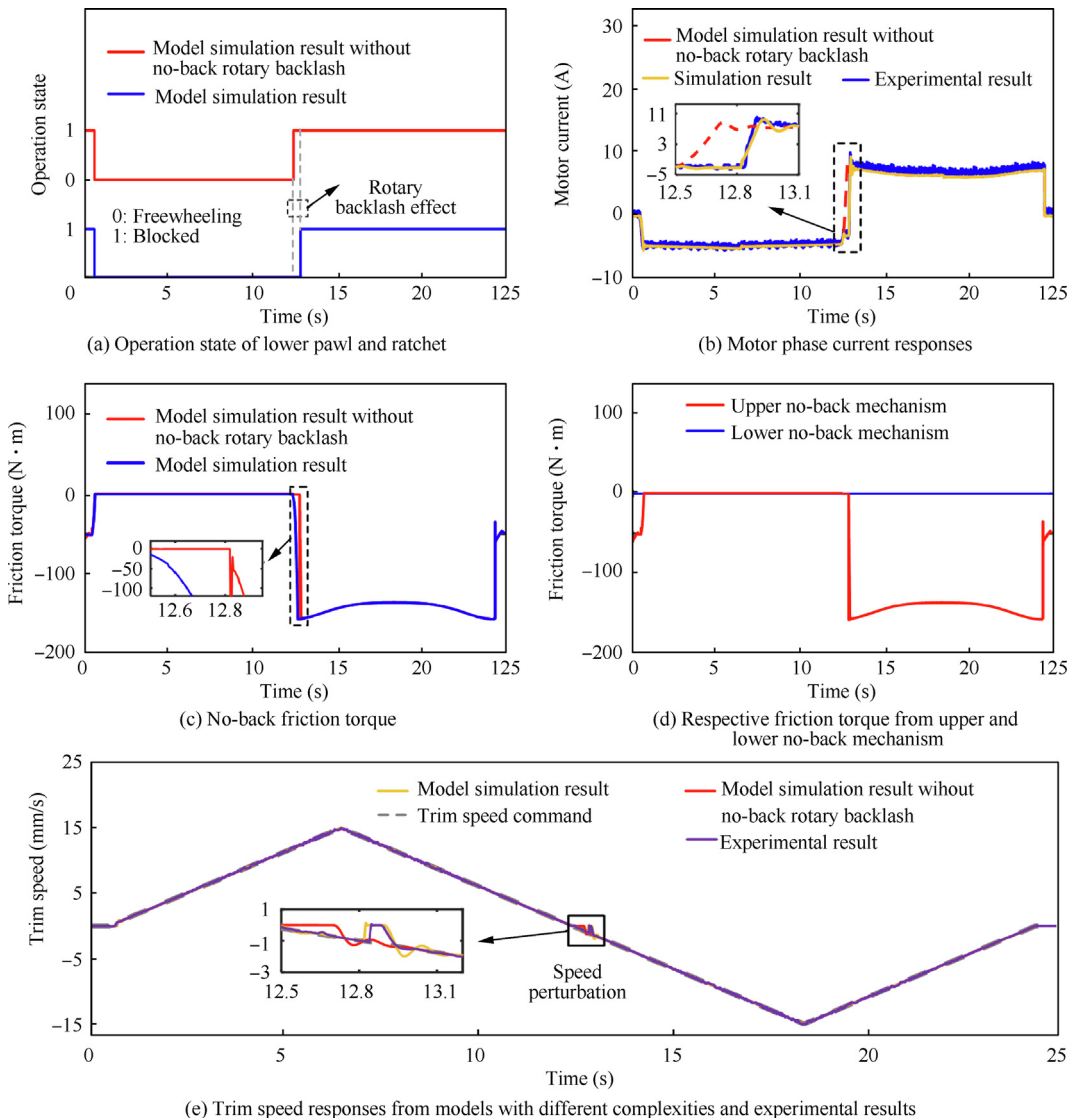
### 5.2. Response to triangular speed command

To address all the potential operating quadrants and conduct the complete working principle test for the no-back mechanism, another operation condition is utilized by applying a triangular trim speed command with an amplitude of 15 mm/s and period of 24 s at time 0.5 s. The external force input is kept constantly tensile (downward) at 29kN. The simulation responses and experimental results, including trim speed feedback, motor phase current, no-back friction, operation states of pawl and ratchet mechanism are depicted in Fig. 15. And the results of the performance indexes are shown in Table 4.

With the trim speed direction variations, the operation mode of the lower pawl ratchet mechanism reverses in Fig. 15 (a). The operation mode of the upper pawl ratchet mechanism maintains freewheeling, since the tensile external force is larger enough to eliminate its inside contact force.

Obviously, combining the friction torque simulation results in Fig. 15 (c) and Fig. 15 (d), the primary friction torque source comes from the friction generated from the lower friction disk. At the same time, the external load switches from opposing into aiding. From Fig. 15 (b) and Table 4, the huge friction torque differences cause that the opposing current amplitude is about 65% of aiding current amplitude, which is consistent with the working principle analysis in section 3. The realistic friction model is utilized rather than a pure coulomb model to handle the no-back friction torque, that is why the experimental results of motor phase current show speed dependent characteristic in Fig. 15 (b).

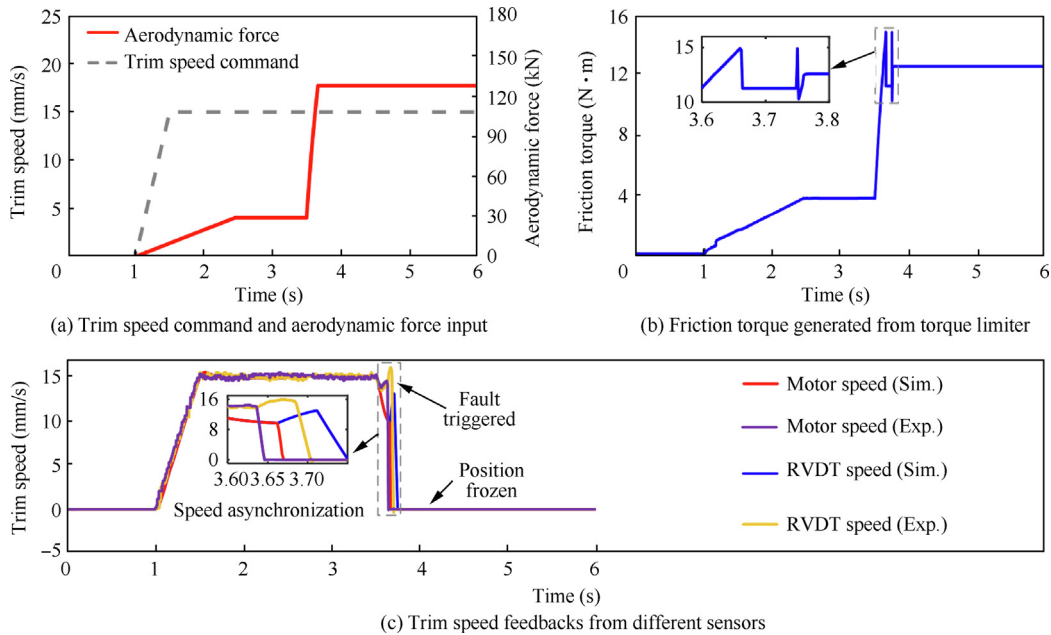
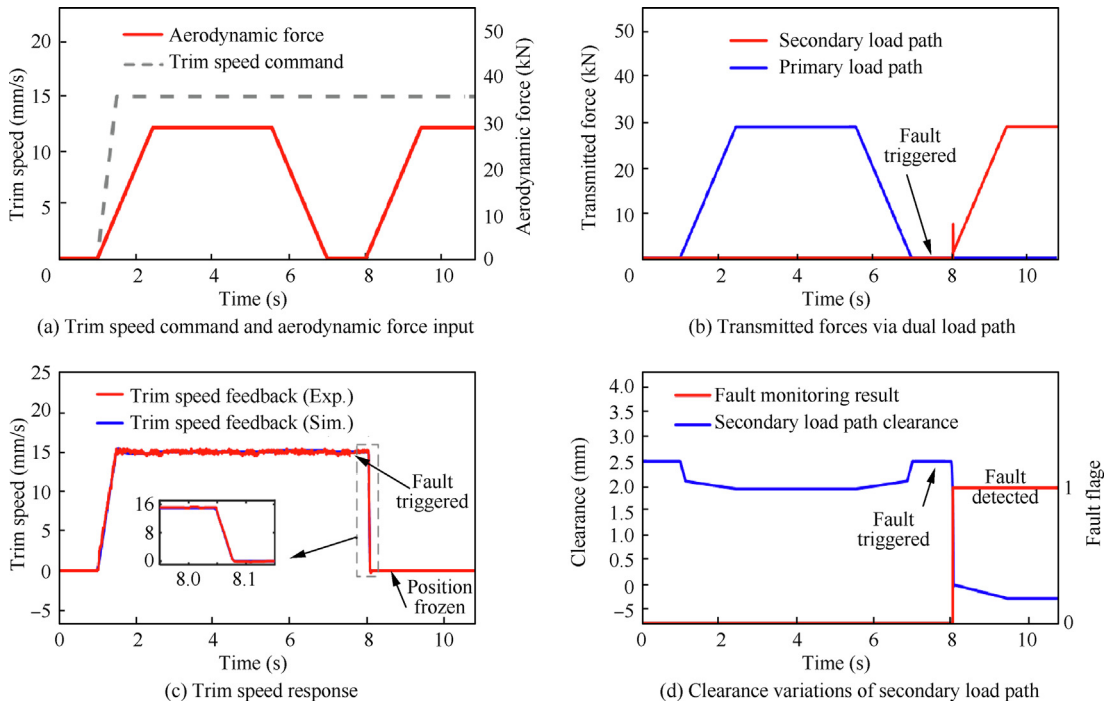
At approximately time 12.5 s, when the trim direction reverses, the operation mode of the lower pawl and ratchet mechanism switches from freewheeling to blocked state, which makes the lower friction disk slip. The friction torque experiences a sudden increase under this aiding load condition in Fig. 15 (c), which causes about 8% maximum following error in Table 4. From Table 4, compared with simulated responses without no-back rotary backlash, these backlash effects intro-



**Fig. 15** Responses from models with different complexities and experimental results under triangular speed.

**Table 4** Simulation and experimental results of dynamic performance indexes under triangular speed.

Item	$t_{bf, 1}$ (s)	$t_{bf, u}$ (s)	$t_{fb, 1}$ (s)	$t_{fb, u}$ (s)	$I_{mo}$ (A)	$I_{ma}$ (A)	$E_{vmax}$ (%)	$E_{vmean}$ (%)
Model simulation results without no-back rotary backlash	0.688	—	12.414	—	-4.98	6.38	4.81	0.02
Model simulation results	0.688	—	12.818	—	-4.98	6.23	8.08	0.02
Experimental results	—	—	—	—	-4.5	7.01	7.85	0.01

**Fig. 16** Responses to jamming fault.**Fig. 17** Responses to primary load path failure.

duce a switching clock delay (close to 40 milliseconds), when corresponding pawl and ratchet mechanism switches its operation mode in Fig. 15 (a). Similarly, this time delay is reflected on the friction torque in Fig. 15 (c) and can be observed in the trim speed and motor phase current experimental results in Fig. 15 (b) and Fig. 15 (e).

### 5.3. Response to crucial actuator faults

#### 1) Response to jamming fault

The control surface is purposely locked by mechanical stop to inject a jamming fault at time 3.5 s. In Fig. 16 (a), when the actuator continues operating, the motor torque output increases rapidly to overcome the huge external force. Consequently, as depicted in Fig. 16 (b), the breakaway friction torque of the torque limiter is eventually overridden. A relative slip occurs between the input shaft and output shaft of torque limiter, which desynchronizes the speed feedbacks by the RVDT and motor position sensors in Fig. 16 (c). Subsequently, the jamming fault can be detected according to the fault diagnosis strategy mentioned in section 3, which commands the engagement of the POB to freeze the surface position. As a consequence, the actuator loses normal actuation function and both actuation channels are turned into the fail/frozen mode.

#### 2) Response to primary load path fault

The primary load path failure is injected by inserting backlash between the upper gimbal and airframe at time 7.5 s. Similarly, the mechanical housing and attachment between the upper gimbal and test rig structure is removed for the same purpose. The simulated and experimental responses of interest are given in Fig. 17. The applied trim speed command and the external load are displayed in Fig. 17 (a). Combining the load variations carried by the dual load paths and the clearances variations of the secondary load path in Fig. 17 (b) and Fig. 17 (d), in normal operation, the secondary load path remains unloaded due to the clearance existence; However, when a primary load path failure occurs, this initial clearance is eliminated to enable the load to be transmitted via the secondary load path.

As addressed in section 3, when the backlash variation measured by the LVDT sensor exceeds the threshold, this fault can be detected by the EMCU, as shown in Fig. 17 (d). Then, the POB receives an engagement command to freeze the surface position, which can be observed from the trim speed responses in Fig. 17 (c). Therefore, the actuator loses normal actuation function and switches both actuation channels to the fail/frozen mode.

## 6. Conclusions

This paper focused on system-level model implementation and dynamic performance assessment of THSA to support the MBSE approach. The main advantages of the proposed THSA model and main contributions are as follows:

- (1) Compared with previous works for EMA modelling, this paper considers detail nonlinear effects of mechanical components with realism, including nonlinear stiffness

and friction effects. The influence of each nonlinear effect is obtained by comparing the system performance differences between models with different complexities. Meanwhile, the established model considers fault-tolerant mechanical load paths and enables to perform fault injections, which provides foundations for the verification of fault-tolerant and fault detection functions.

- (2) The influence on system performance of backlash of mechanical load path is analyzed. The extra axial displacement/velocity caused by this nonlinear compliance effect is considered to modify the normal compliance model and tangential friction model of the screw-nut mechanism. When the aerodynamic force amplitude is not large enough to eliminate the initial clearance, the poor structural stiffness introduces oscillation and overshoot in the surface speed simulated response, which is confirmed by the experimental results.
- (3) The influences on system performance of friction and backlash of no-back mechanism are investigated. When the operation state of pawl and ratchet mechanism varies from freewheeling into the blocked state, the occurrence of relative slip leads to a sudden increase of friction torque. In addition, a circumferential clearance must be eliminated, before the ratchet wheel and pawl achieve active contact. The observed speed disturbance and response delays prove the importance of considering both nonlinear no-back friction and compliance effects.
- (4) The working principle analysis about how trim direction, load direction and magnitude determine the operation state and friction magnitude of each (upper and lower) no-back mechanism, is detailed proposed and validated by experimental results. When the actuator is active, the upper and lower pawl and ratchet mechanisms share different operation modes, and both are determined by the rotation directions of screw shaft, if the residual preload force still exists. However, if the actuator works under opposing load and the load force is larger enough to eliminate the preload force, both upper and lower ratchet operate in the freewheeling mode. Different operation state s and load directions combinations lead to different torque characteristics and current demands under aiding or opposing load.

## Declaration of Competing Interest

The authors declare that they have no known competing financial interests or personal relationships that could have appeared to influence the work reported in this paper.

## Acknowledgements

This work was supported by the National Natural Science Foundation of China (No. 52275062) and the Fundamental Research Funds for the Central Universities of Beihang University (YWF-22-L-912).

## References

1. Rosero JA, Ortega JA, Aldabas E, et al. Moving towards a more electric aircraft. *IEEE Aerosp Electron Syst Mag* 2007;22(3):3–9.

2. D. Arriola and F. Thielecke, Design of fault-tolerant control functions for a primary flight control system with electromechanical actuators, In: *Proceedings of the IEEE Autotestcon Conference*; 2015 Nov. 02–05, 2015, Maryland; USA, 393–402.
3. Botten SL, Whitley CR, King AD. Flight control actuation technology for next-generation all-electric aircraft. *Technol Rev* 2000;8:55–68.
4. Wang Y, Shen T, Tan C, et al. Research status, critical technologies and development trends of hydraulic pressure pulsation attenuator. *Chin J Mech Eng-EN* 2021;34(1):125–41.
5. Zhao J, Fu Y, Li Y, et al. Flow characteristics of integrated motor-pump assembly with phosphate ester medium for aerospace electro-hydrostatic actuators. *Chin J Aeronaut* 2023;36(9):392–407.
6. Garcia A, Cusido I, Rosero JA, et al. Reliable electro-mechanical actuators in aircraft. *IEEE Aerosp Electron Sys. Mag* 2008;23(8):19–25.
7. Qiao G, Liu G, Shi Z, et al. A review of electromechanical actuators for more/all electric aircraft Systems. *Proc Inst Mech Eng Part C-J Eng Mech Eng Sci* 2017;232(22):4128–51.
8. Aerospace SAE. Trimmable horizontal stabilizer actuator descriptions: SAE AIR6052. *SAE. International* 2011;1–38.
9. Rito GD, Luciano B, Borgarelli N, et al. Model-based condition-monitoring and jamming tolerant control of an electro-mechanical flight actuator with differential ball screws. *Actuators* 2021;10(9):230.
10. Mhenni F, Nguyen N, Choley JY. SafeSysE: a safety analysis integration in systems engineering approach. *IEEE Syst J* 2018;12(1):161–72.
11. Eigner M, Gilz T, Zafirov R. Proposal for functional product description as part of a PLM solution in interdisciplinary product development. *Proceedings of 12th International Design Conference; Dubrovnik, Croatia*; 2012. p. 1667–76.
12. Siala H, Mhenni F, Choley JY, et al. Toward a robust design of an aileron electromechanical actuator: sensitivity analysis and parametric tolerancing using a variational approach. *IEEE Syst J* 2020;14(3):3977–86.
13. Fu J, Maré J-C, Fu Y. Modelling and simulation of flight control electromechanical actuators with special focus on model architecting, multidisciplinary effects and power flows. *Chin J Aeronaut* 2017;30(1):47–65.
14. Karam W, Maré J-C. Modelling and simulation of mechanical transmission in roller-screw electro-mechanical actuators. *Aircr Eng Aerosp Technol* 2009;81(4):288–98.
15. Arriola D, Thielecke F. Model-based design and experimental verification of a monitoring concept for an active-active electromechanical aileron Actuation System. *Mech Syst Signal Proc* 2017;94:322–45.
16. Giangrande P, Galassini A, Papadopoulos S, et al. Considerations on the development of an electric drive for a secondary flight control electromechanical actuator. *IEEE Trans Ind Appl* 2019;55(4):3544–54.
17. Bertolino AC, Sorli M, Jacazio G, et al. Lumped parameters modelling of the EMAs' ball screw drive with special consideration to ball/grooves interactions to support model-based health Monitoring. *Mech Mach Theory* 2019;137:188–210.
18. Fu J, Zheng C, Maré J-C, et al. Virtual prototyping of electrical THSA focused on mechanical power transmission functions. *Proceedings of the 32nd International Congress of the Aeronautical Sciences (ICAS)*; Shanghai, China; 2021. p. 1–13.
19. Johnsen S, Thielecke F. Integration analysis of trimmable horizontal stabilizer actuators and technology evaluation. *CEAS Aeronaut J* 2011;2(1–4):11–9.
20. Maré J-C. *Aerospace actuators volume 2: signal and power by wire*. 1st ed. London: John Wiley & Sons, Inc; 2017. p. 32–5.
21. Fu J, Maré J-C, Yu L, et al. Multi-level virtual prototyping of electro-mechanical actuation system for more electric aircraft. *Chin J Aeronaut* 2018;31(5):892–913.
22. Clément C, Fu J, Maré J-C. Bond graphs aided development of mechanical power transmission for aerospace electromechanical actuators. *Proceedings of the 12th International Conference on Bond Graph Modeling and Simulation*; 2016 July 24–27; Montreal; Canada; 2016. p. 221–8.
23. Lin MC, Ravani B, Velinsky SA. Kinematics of the ball screw mechanism. *J Mech Des* 1994;116(3):849–55.
24. Maré J-C. Requirement-based system-level simulation of mechanical transmissions with special consideration of friction, backlash and preload. *Simul Model Pract Th* 2016;63:58–82.
25. Balaban E, Bansal P, Stoelting P, et al. A diagnostic approach for electro-mechanical actuators in aerospace systems. *Proceedings of the IEEE Aerospace Conference*; 2009 March 7–14; MT, USA; 2009. p. 1–13.
26. Wang X, Wang Z, Xu Z, et al. Comprehensive diagnosis and tolerance strategies for electrical faults and sensor faults in dual three-phase PMSM drives. *IEEE Trans Power Electron* 2019;34(7):6669–84.
27. Qi Y, Bostanci E, Gurusamy V, et al. A comprehensive analysis of short-circuit current behavior in PMSM interturn short-circuit faults. *IEEE Trans Power Electron* 2018;33(12):10784–93.
28. Gu JX, Albarbar A, Sun X, et al. Monitoring and diagnosing the natural deterioration of multi-stage helical gearboxes based on modulation signal bispectrum analysis of vibrations. *International Journal of Hydro-mechatronics* 2021;4(4):309–30.
29. Liu D, Shi J, Liao Z, et al. Prognostics and health management for electromechanical system: a review. *Journal of Advanced Manufacturing Science and Technology* 2022;2(4):2022015.
30. Wang X, Wang S, Yang Z, et al. Active fault-tolerant control strategy of large civil aircraft under elevator failures. *Chin J Aeronaut* 2015;28(6):1658–66.
31. Zhang W, Fu J, Fu Y, et al. System performance analysis for trimmable horizontal stabilizer actuator focusing on nonlinear effects: based on incremental modelling and parameter identification methodology. *Sensors* 2021;21(19):6464.